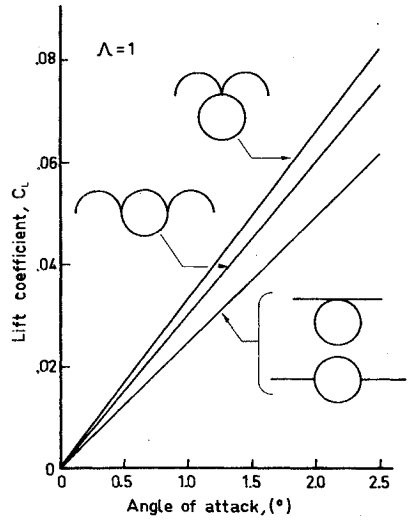

Fig. 3 Comparison of lift coefficient for cylindrical and flat wing-body combinations.

the x_3-axis and asymptotically approach $\pm 1/2r$ as y_3 decreases toward infinity. The intersection point between the wing and fuselage in the Z_2-plane is thereby greatly expanded in the Z_3-plane and leads to a more detailed representation of the complex potential in this region. The rectilinear flow at infinity in the Z_2-plane becomes a doublet pointing downward at the origin in the Z_3-plane.

The two wings in the Z_3-plane can be represented by two symmetric vortex sheets. Since the y_3-axis must be a streamline, the vortex strength at corresponding y_3's on both wings must have the same magnitude but opposite sense, according to the reflection principle. The complex potential resulting from the two vortex sheets and the doublet at the origin can be expressed as

$$w(Z_3) = i\int_0^\infty \gamma(\zeta)\ln\left[\frac{Z_3 - Z_w(\zeta)}{Z_3 + \bar{Z}_w(\zeta)}\right]d\zeta - \frac{i\alpha}{Z_3} \tag{5}$$

where ζ is the distance along the wing (vortex sheet) starting at $\pm 3/8r$, $\gamma(\zeta)$ is the vortex strength distribution and $Z_w(\zeta)$ is the complex variable describing the location of the wing in the Z_3-plane. The velocity component normal to wings must be zero in order that the wings be streamlines so the following condition

$$V_n = Im[Z_w'(\zeta)(dw/dZ_3)|_{Z_w}] = 0 \tag{6}$$

must be satisfied everywhere along the wing. This leads to an integral equation for $\gamma(\zeta)$ which was solved numerically by subdividing the vortex sheet into a series of discrete vortices. Having determined the vortex strength distribution, the residue is obtained by expanding the complex potential in a Laurent series about $Z_3 = 0$ and writing Z_3 as a function of Z_1. The result is

$$a_{-1}(z_B) = i\alpha r^2 - 2i\int_0^\infty \gamma(\zeta)(Re[Z_w]/|Z_w|^2)\,d\zeta \tag{7}$$

which gives a numerical value for the residue of

$$a_{-1}(Z_B) = 5.40\,i\alpha r^2 \tag{8}$$

The wings in the Z_2-plane do not deviate significantly from the semicircles represented by dashed lines in Fig. 2. If, indeed, the wings were semicircles, the inversion mapping would have yielded the two semi-infinite slits indicated also by the dashed lines in the Z_3-plane. It would then have been possible to transform the wings onto the x-axis using the Schwartz-Christoffel transformation, the fuselage still being two slits along the y-axis. In this case the doublet at the origin in the Z_3-plane would have become a doublet on the y-axis directed in the negative y-direction so the flowfield analysis would have reduced to the simple problem of a doublet near a wall. Since the actual wings in the Z_2-plane approximate semicircles, the flowfield solution for the semicircular wings was obtained and the residue evaluated to serve as a check on the above result. The residues differed by less than 5%, that for the actual wing being the smaller of the two.

The lift force is predicted by substituting the residue into Eq. 2. The result is

$$L = 9.80\pi\rho U_\infty{}^2 r^2\alpha \tag{9}$$

The wing span is six times the body radius so the lift force can be written as

$$L = (9.80\pi/36)\rho U_\infty{}^2 b^2\alpha \tag{10}$$

The lift coefficient, then, is

$$C_L = 1.71\Lambda\alpha \tag{11}$$

and the lift curve slope has the value of

$$C_{L_\alpha} = 1.71\Lambda \tag{12}$$

Spreiter[4] has shown that flat wings of the same span mounted on the side of the fuselage have a lift curve slope of 1.41Λ. Thus, the cylindrical wings produce over 20% more lift than the flat wings at the same angle of attack.

It is interesting to compare graphically the predicted lift coefficient vs angle of attack for cylindrical and flat wing-body combinations as illustrated in Fig. 3. Both the top-mounted and side-mounted cylindrical wings outperform their flat-wing counterparts. The highest lift curve slope is obtained for the top-mounted cylindrical wings. However, the highest lift is obtained for the side-mounted wings since the span is increased from two to three times the body diameter. The comparatively higher lift curve slope of the cylindrical wings suggests their suitability for high performance cruise vehicles which can be packaged in a limited space. Experimental verification of the predicted lift characteristics and measurements of other aerodynamic parameters, such as drag, are necessary before the relative merits of cylindrical wings can be realistically assessed.

References

[1] Fournier, P. G., "Aerodynamic Characteristics at Low Speed of a Reentry Configuration Having Rigid, Tractable, Conical Lifting Surfaces," TN D-622, 1960, NASA.

[2] Crowell, K. R. and Crowe, C. T., "Prediction of the Lift and Moment on a Slender Cylinder-Segment Wing-Body Combination," *Journal of the Royal Aeronautical Society*, Vol. 77, No. 750, 1973, pp. 295–298.

[3] Ward, G. N., *Linearized Theory of High Speed Flow*, Cambridge Univ. Press, Cambridge, Mass., 1955.

[4] Spreiter, J. R., "The Aerodynamic Forces on Slender Plane and Cruciform-Wing and Body Combination," Rept. 962, 1950, NACA.

Simulation of Real-Gas Effects for Mars Entry

JAMES L. HUNT,* ROBERT A. JONES,* AND RAYMOND E. MIDDEN†
NASA Langley Research Center, Hampton, Va.

Nomenclature

A = reference area, $\pi R_B{}^2$
C_D = drag coefficient, $D/q_\infty A$

Received July 19, 1973; revision received September 6, 1973.
Index categories: Supersonic and Hypersonic Flow; Entry Vehicles and Landers; Entry Vehicle Testing.

* Aerospace Technologist, Hypersonic Aircraft Systems Research Branch, Hypersonic Vehicles Division.
† Aerospace Technologist, Gas Radiation Section, Space Systems Division.

C_L = lift coefficient, $L/q_\infty A$
C_m = pitching-moment coefficient, $m/q_\infty AR_B$
D = drag
L = lift
m = pitching-moment
M = freestream Mach number
P = pressure
q_∞ = freestream dynamic pressure
R_B = maximum base radius
γ = ratio of specific heats
ρ = density
ϕ = angular displacement from windward ray of forebody

Subscripts
1 = freestream static conditions
2 = static condition behind normal shock
t_2 = stagnation condition behind normal shock

AS the Viking aeroshell enters the Martian atmosphere at hypersonic speeds, the gas molecules (CO_2) that pass through the bow shock are excited to higher vibrational and chemical energy modes. This excitation increases the degrees of freedom of the gas in the shock layer provided equilibrium exists and dissociation is not driven near completion. Since both of these conditions will exist in the shock layer during the Martian entry, the ratio of specific heats of the gas in this layer will be much lower than that in the freestream. A large amount of the energy that would normally be used in increasing the static temperature behind the bow shock is thus used in exciting vibrational energy levels or dissociating the real-gas molecules. As additional energy is absorbed by the gas molecules entering the shock layer, the conservation laws and the thermophysics of the gas dictate certain changes in the forebody flow. The static temperature, speed of sound, and velocity in the real-gas shock layer are reduced. The static pressure is increased slightly. The density is increased considerably and the shock layer thickness is reduced in proportion to this increase.

At supersonic and hypersonic speeds, the aerodynamic characteristics including the lift, drag, moments, and stability of blunt configurations such as the Viking aeroshell are determined almost exclusively by the forebody flowfield. Several previous investigators[1-4] have shown that for very high speeds the inviscid forebody flow on such configurations, while independent of Mach number, are strongly dependent on real-gas effects such as excitation of vibrational energy levels or dissociation. These real-gas effects have been shown[1-4] to correlate as a function of the density ratio across the bow shock (ρ_2/ρ_1).

The changes in aerodynamic characteristics due to real-gas effects associated with high-speed flight (characterized by large shock density ratios) are primarily the result of changes in surface pressures acting on the forebody. The surface pressures are affected by a change in shock density ratio (real-gas effects) in two ways[2]: First, the level of pressure at the stagnation point relative to freestream dynamic pressure is changed, and second, the distribution of surface pressure relative to stagnation-point pressure is changed.

The density-ratio effect on the stagnation-point pressure level can be estimated by considering the flow of a perfect gas about a blunt body. Conserving mass and momentum across a normal shock, considering incompressible flow from the shock to the stagnation point, and neglecting the freestream static pressure compared to that in the shock layer, results in the equation[2]

$$P_{t_2}/(\tfrac{1}{2}\rho_1 u_1^2) = 2 - 1/(\rho_2/\rho_1) \quad (1)$$

This approximate equation which applies for real as well as ideal gases shows that the nondimensional stagnation pressure level on a blunt body is essentially a function only of the shock density ratio and will increase slightly with increasing shock density ratio. Doubling the density ratio increases the pressure by 5%.

In order to determine the factors influencing the pressure distribution on blunt bodies, a one-strip integral method was exercised[2] over several different types of blunt body configurations at various values of Mach number and specific heat ratio and thus at various density ratios. The results indicated that the pressure distribution on each of these blunt-body configurations depended essentially only on the shock density ratio for Mach numbers of 6 or larger. These results[2] are restricted to bodies on which sonic velocities occur at the point of maximum body radius.

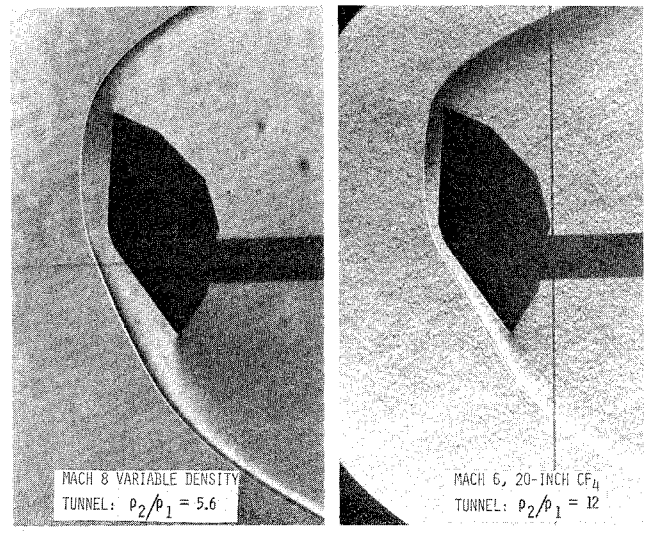

Fig. 1 Real-gas effects on Viking aeroshell bow shock.

Since the shock density ratio dictates the pressure level and distribution on blunt bodies, a simple way to simulate inviscid real-gas effects on such configurations is to test in a substitute gas flow which provides the correct density ratio without any dissociation. For an ideal gas[5] the expression for the density ratio across a normal shock is a function of gamma and Mach number

$$\rho_2/\rho_1 = (\gamma+1)M^2/[(\gamma-1)M^2+2] \quad (2)$$

An effective value of gamma, γ_e, can be defined as the substitute gas value which gives the correct normal shock density ratio using the freestream Mach number, M, in Eq. (2). The variation of shock density ratio with shock angle in flight is such that matching the normal shock density ratio also insures matching of the oblique shock density ratios for shock angles above 40°.

The Viking aeroshell entering the mean Mars model atmosphere (Viking Aerophysics Data Book, Martin Marietta Corp.) at an entry angle of −17°, an entry velocity of 15,175 ft/sec, and an L/D of 0.18 for an angle of attack (α) of 11.2°, encounters peak dynamic pressure at a normal shock density ratio of 13.4 (assuming equilibrium). In order to assess the trends of the real-gas effects on the aerodynamics of the aeroshell, pressure tests were conducted on a 4-in.-diam model in the Langley Mach 8 variable density air tunnel at a normal shock density ratio of 5.6 and in the Langley 20-in., Mach 6, CF_4 tunnel at a shock density ratio of 12. The angle of attack of these tests was from 0 to 16°.

Schlieren photographs of the aeroshell in both facilities at 16° angle of attack are shown on Fig. 1. The bow shock is much closer to the body in CF_4 at a density ratio of 12 than in air at a density ratio of 5.6. Also note the straightness of the shock on the more leeward surface of the forebody in CF_4 compared to the bulge of the shock along this surface in air. This is the surface from which the aeroshell receives its lift.

The pressure distributions obtained in both sets of tests on the aeroshell forebody at 11.2° angle of attack (trim angle) are shown in Fig. 2 for 12 conical rays. A comparison of the air and CF_4 data along the windward meridian ($\phi = 0$, $\phi = 180$) seems to indicate that the lift is less and the pitching moment greater (toward $\alpha = 0$) at the higher shock density ratio (CF_4) since the pressure distribution is driven closer to the Newtonian

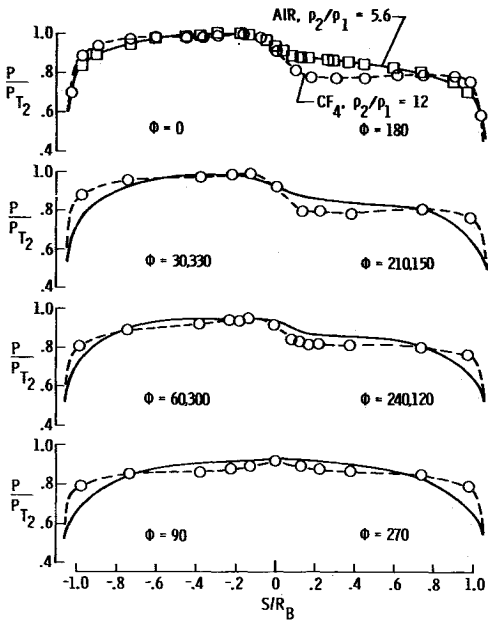

Fig. 2 Pressure distributions on forebody of Viking aeroshell at 11.2° angle of attack.

level on the lifting surface of the aeroshell. This could be misleading when one notes that the pressures for the higher shock density ratio gas (CF_4) are higher than that of air near the outer edge of the axisymmetric vehicle where the area is large.

Pressure data on the aeroshell afterbody were also obtained in these tests; however, for Mars entry the real-gas flow of dissociated CO_2 in the expansion to the wake will probably be frozen or finite-rate resulting in a much higher effective gamma for the afterbody flow than for the forebody. The afterbody pressures depend strongly on the specific heat ratio, and the influence of this ratio increases with increasing Mach number.[6] Thus, while the CF_4 data provide an excellent simulation of the forebody shock shapes and forebody pressures resulting from real-gas effects during Mars entry, it does not simulate the pressures on the afterbody. Therefore, to obtain a realistic indication of real-gas effects for Mars entry, a comparison of the integrated pressure data over just the forebody at hypersonic Mach numbers for different shock density ratios should be used.

Integrating the pressure distributions at 11.2° angle of attack over the forebody of the axisymmetric vehicle gives the following aerodynamic coefficients, where the pitching moment is calculated about a horizontal line normal to the axis of symmetry at the extended apex (sharp cone) of the vehicle. The conventional coefficients (C_L, C_D, and C_m), which include the change

Table 1 Aerodynamic coefficients

	AIR, $M = 8$ $\rho_2/\rho_1 = 5.6$ $P_{t_2}/q_\infty = 1.84$	CF_4, $M = 6$ $\rho_2/\rho_1 = 12$ $P_{t_2}/q_\infty = 2.00$	Percent change Air → CF_4
C_L	0.267	0.294	10.1
$L/P_{t_2}A$	0.145	0.147	1.4
C_D	1.474	1.630	10.6
$D/P_{t_2}A$	0.801	0.816	1.7
L/D	0.181	0.180	−0.6
C_m	0.021	0.028	33.3
$m/P_{t_2}A(2R_B)$	0.0114	0.0140	22.8

in the total pressure behind the shock relative to the dynamic pressure of the freestream, are restricted to points on the Viking trajectory where the ratio P_{t_2}/q_∞ is the same as that shown for the tests. The aerodynamic forces nondimensionalized by the total pressure behind the shock include only the effects of the forebody pressure distribution and can probably be used over a moderate shock density ratio range.

As shown above, the lift and drag are about 11% higher in CF_4 than air so that L/D remains essentially the same at the two different shock density ratios. The pitching moment is 33% higher (toward $\alpha = 0$) in CF_4 than in air at the design trim angle of attack of 11.2°; however, this difference should only be used as an indicator and not an absolute value since the pitching moment is extremely sensitive to data fairing errors. A decrease in the trim angle of attack will reduce lift, further increase the drag, and thus result in a shorter range than that predicted from hypersonic air data.

References

[1] Anon., "Comparative Studies of Conceptual Design and Qualification Procedures for a Mars Probe/Lander. Volume V: Subsystem and Technical Analyses—Book 2: Aeromechanics and Thermal Control," AVSSD-006-66RR (Contract NAS1-5224), May 11, 1966, AVCO Corp., Wilmington, Mass.

[2] Jones, R. A. and Hunt, J. L., "Use of Tetrafluoromethane to Simulate Real-Gas Effects on the Hypersonic Aerodynamics of Blunt Vehicles," TR R-312, June 1969, NASA.

[3] Krumins, M. V., "Drag and Stability of Various Mars Entry Configurations," IAF Paper RE138, Oct. 1968, 19th Congress of the International Astronautical Federation, New York.

[4] Allison, D. O. and Bobbitt, P. J., "Real-Gas Effects on the Drag and Trajectories of a Nonlifting 140-Degree Conical Aeroshell During Mars Entry," TN D-6240, 1971, NASA.

[5] Ames Research Staff, "Equations, Tables, and Charts for Compressible Flow," Rept. 1135, 1953, NACA.

[6] Mishin, G. I. and Shelud-ko, Iu, "Dependence of Base Pressure on the Ratio of Specific Heats at Supersonic Velocities," *Zhurnal Tekhnicheskoi Figiki*, Vol. 42, Oct. 1972, pp. 2208–2212.